Available online at www.sciencedirect.com
ScienceDirect
Trans. Nonferrous Met. Soc. China 33(2023) 3319−3331
Transactions of Nonferrous Metals Society of China
www.tnmsc.cn

Microstructure and properties of Ti60 alloy by laser solid forming and ultrasonic impact hybrid manufacturing

Wen-jing CHEN[1], Chun-ping HUANG[1], Feng-gang LIU[1], Ren-yu LIANG[1], Fen-cheng LIU[1], Hai-ou YANG[2]

1. National Defense Key Discipline Laboratory of Light Alloy Processing Science and Technology, Nanchang Hangkong University, Nanchang 330063, China;
2. Key Laboratory of Metal High Performance Additive Manufacturing and Innovative Design, Northwestern Polytechnical University, Xi'an 710072, China

Received 22 March 2022; accepted 1 September 2022

Abstract: The hybrid manufacturing of laser solid forming (LSF) and ultrasonic impact treatment (UIT) was used to improve the structure and properties of Ti60 alloy by strengthening the surface layer-by-layer. The microstructure, mechanical properties, and burn resistance of LSFed Ti60 samples before and after UIT by SEM, TEM, and XRD were analyzed and compared. The results showed that the grains of LSFed Ti60 alloy were refined and metallurgical defects were reduced after the UIT process. Meanwhile, the deposited layer was severely deformed after UIT and nanocrystals were formed on the surface. In addition, the microhardness of the deposition layer surface increased and the residual stress changed from tensile stress to compressive stress. The area of the ablation hole was reduced by 21% and the proportions of Mo, Nb, and Zr elements increased. In summary, hybrid manufacturing of LSF and UIT can improve the microstructure and properties of LSFed Ti60 samples.

Key words: Ti60 alloy; ultrasonic impact treatment; laser solid forming; microstructure; mechanical properties; burn resistance performance

1 Introduction

High-temperature titanium alloys are widely used in the manufacture of aero engine high-pressure compressor discs, blades, casing, and other components to reduce engine weight and improve the thrust-weight ratio [1]. Ti60 alloy is a near-α high-temperature titanium alloy [2] with a service temperature set at 600 °C [3]. However, Ti60 alloy is sensitive to the deformation temperature, strain, and other process parameters and has the characteristics of low thermal conductivity and high chemical activity [4]. Because hot processing of Ti60 alloys is difficult, there is an urgent need to find a novel preparation technology, therefore advanced additive manufacturing (AM) technology [5] is adopted. Laser solid forming (LSF) [6] is a typical AM technology that integrates rapid prototyping manufacturing and laser cladding [7,8]. This promising technology shines brightly on the forming and repair of dense metal parts in the aerospace field.

However, three problems still restrict the forming quality of LSFed titanium alloy workpieces. First, columnar crystals are formed during the LSF process [9]. The crystal anisotropy caused by columnar crystal morphology greatly limits its application in the complex stress field. Second, metallurgical defects [10], such as porosity, greatly reduce the fatigue performance of titanium alloy. The third is residual stress [11]. Due to the complex

Corresponding author: Chun-ping HUANG, Tel: +86-13576030335, E-mail: hcp98106@163.com;
Hai-ou YANG, Tel: +86-13991355030, E-mail: yanghaiou@nwpu.edu.cn
DOI: 10.1016/S1003-6326(23)66336-8

thermal cycling and thermal accumulation in the LSF, the thermal stress without releasing in the Ti60 alloy sample will be transformed into residual stress. These problems not only limit the application of LSFed Ti60 alloy parts in the aerospace field but also bring certain hidden dangers and economic losses. According to relevant mainstream research, there are two common methods to achieve grain refinement and improve the strength and plasticity of materials: metamorphic and deformation. In deformation treatment, the introduction of ultrasonic impact treatment (UIT) for surface strengthening treatment [12,13] has attracted the attention of international researchers. Compared with other traditional surface treatment methods, such as rolling [14] and shot peening (SP) [15−16], UIT can obtain nanolayers on metal surfaces with the advantages of low cost, high efficiency, no pollution, and good controllability [17]. The UIT device uses powerful energy to push the impact head against metal surfaces, resulting in large compressive plastic deformation of the metal surface. At the same time, UIT changes the original stress field and beneficial compressive stress is generated. Under the impact of high energy, the temperature of the metal surface increases and cools rapidly, which changes the surface metal structure and strengthens the surface [18].

LESYK et al [19] used barrel finishing (BF), ultrasonic shot peening (USP), SP, and UIT techniques to improve the surface layer properties of SLM. The results show that the multi-pin UIT process is considered more effective and suitable for industrial scale. YU et al [20] used an HJ−III ultrasonic impact processor to perform surface treatment of MB8 wrought magnesium alloy. The results show that the grains on the surface of MB8 are highly refined, and the microhardness and wear resistance of the surface layer are significantly improved. YANG et al [21] investigated the residual stresses in deposited samples after UIT-assisted arc additive manufacturing (WAAM) of TC4 alloy. The results show that UIT has a significant effect on residual stress. The residual stress of the UITed samples is lower than that of the deposition. TRUDEL et al [22] extended the application of UIT to Ti−6Al−4V manufactured by direct metal laser sintering technology. The results show that the optimal fatigue life increases by 150% compared to untreated parts. DONOGHUE et al [23] adopted UIT to treat LSFed TC4 deposits alternately and observed and compared the size and orientation of the primary α phase in different UIT processes through electron back- scattered diffraction (EBSD). In a subsequent study, they rolled the formed layer and found that the deposited layer was severely deformed and the grain size became finer. Researchers around the world have conducted various surface strengthening experiments on the defects of titanium alloy additively manufactured parts. However, the existing studies have generally focused on the surface strengthening of the most superficial layer of the additively manufactured metal, and the effect of UIT + LSF on the layer-by-layer strengthening of the Ti60 alloy surface has rarely been investigated.

Therefore, combined with the outstanding advantages of UIT in material strengthening, the evolution of microstructure, phase, hardness, and burn resistance properties of LSFed Ti60 alloy after UIT was studied. This research work may provide data support and reference for the practical application of Ti60 alloy and the development of ultrasonic impact online assisted LSF technology.

2 Experimental

In this experiment, annealed TC4 titanium alloy was used as the base material, and Ti60 powder prepared by plasma rotating electrode process (PREP) was used as the deposited material, and the chemical composition of Ti60 alloy is shown in Table 1.

Table 1 Chemical composition of Ti60 alloy (wt.%)

Al	Sn	Zr	Ta	Mo	Nb	Si	Ti
5.6	3.8	3.2	1	0.5	0.4	0.35	Bal.

An IPG laser additive manufacturing system was used in the experiment. The laser type was YLS−4000, and the operating platform was an MH24 six-axis Yaskawa robot. The laser wavelength was 1070 nm, the rated output power was 4 kW, and the fiber diameter was 800 nm. The process parameters are shown in Table 2.

The model of UIT equipment was kzuit−20c, and the parameters were as follows: the operating frequency (19.8±0.2) kHz, the maximum output power of the transducer 3 kW, the maximum output

amplitude 100%, the maximum current 5 A, and the tool head specifications *d*6 mm. An impact pressure of 0.05 MPa was used in the UIT control experiment. The optimal UIT process parameters are determined in Table 3.

Table 2 Technological parameters of LSFed Ti60 alloy

Laser power/ kW	Scanning rate/ (m·min^{-1})	Spot diameter/ mm	Powder feeding rate/ (g·min^{-1})	Overlap rate/ %
1.0	0.7	2.4	7.0	45.00

Table 3 UIT process parameters

Impact speed/ (m·min^{-1})	Impact times	Offset distance/ mm	Impact needle diameter/ mm	Air pressure/ MPa
0.60	4	1.00	6.00	0.05

The forming process of the LSF experiment is shown in Fig. 1(a). Before LSF, the Ti60 powder was dried in an oven before the experiment to remove moisture. The samples were polished and cleaned with acetone and alcohol wool to eliminate interfering factors. In the experiment, the instrument moved in three axes and fed powder coaxially. In Fig. 1(c), scanning was carried out along the thickness direction according to the reciprocating scanning path and ended after scanning 8 layers.

The schematic diagram of UIT is shown in Fig. 1(b). The UIT system includes an impact head, impact needle, Ti60 deposited layer, and fixture [24]. The schematic diagram of the impact head shows the structure of the impact needle. The UIT was carried out in a reciprocating way, and the cooling method was air-cooled. The LSFed Ti60 alloy deposited layer was taken as the test object. Before testing, the sample was fixed and UIT was performed according to the trajectory preset in Fig. 1(c). Each layer of the sample was treated with UIT and ended after 8 layers were processed.

Figure 1(c) shows the working process of the LSF + UIT working system. A Ti60 deposition layer was added to the substrate by LSF and the sample was removed from the LSF operating table after it was air-cooled to room temperature. Applying UIT to the deposited layers of LSF resulted in severe deformation and fragmentation of the columnar crystals formed during LSF. In addition, tensile residual stresses were released. At the end of the UIT process, the surface of the deposited layer was cleaned to continue with the LSF experiment. After cooling, it entered the next working cycle.

The LSFed Ti60 samples need to be analyzed and processed for microstructure. The middle section was taken by wire-cut electrical discharge machining (WEDM) equipment. The roughness was measured with a roughness profiler (JB−6C). After that, the samples were inlaid with an XQ−1 inlay machine. The sample was roughened by SiC

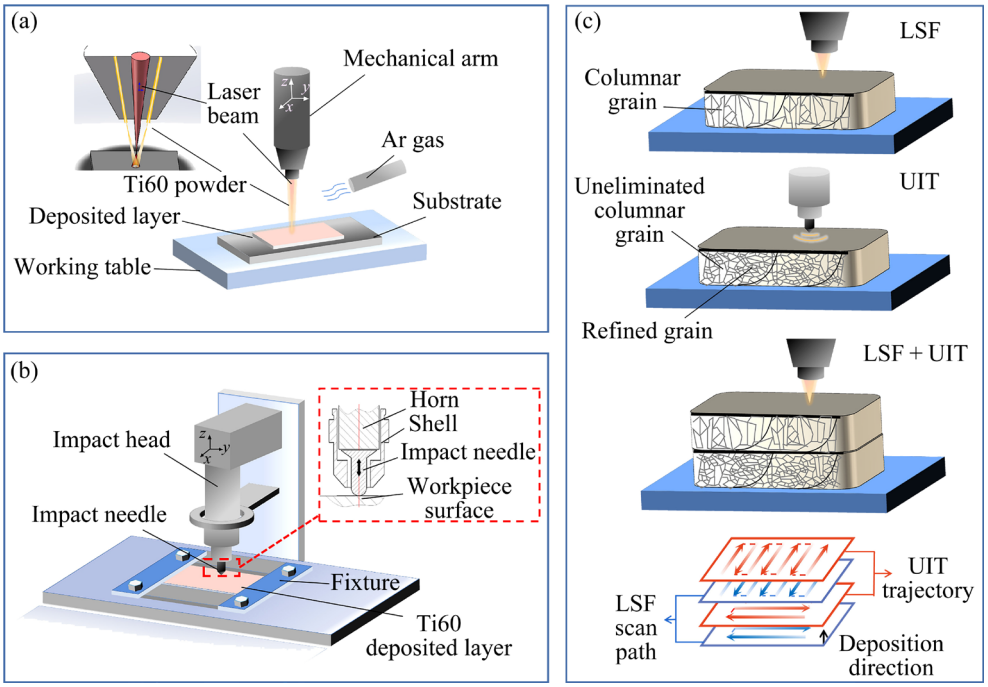

Fig. 1 Schematic diagrams of LSF + UIT working system: (a) LSF; (b) UIT; (c) UIT + LSF and scanning mode

sandpaper and polished on an HYP−1 metallographic sample polishing machine to obtain a mirror surface. After polishing etching, a 4XB−TV metallographic microscope was used to observe the microstructure distribution characteristics and grain size of the top area before and after UIT. The surface area of the sample with a diameter of 3 mm and a thickness of 0.1 mm was selected to prepare the thin section sample. The grain size was observed by a Talos F200x field emission transmission electron microscope (TEM). Phase analysis of LSFed Ti60 alloy samples was carried out by X-ray diffraction (XRD, D8 ADVANCED−A25) techniques before and after UIT. A Qness A10 Vickers microhardness tester was used to measure the hardness in the thickness direction. Vickers indentation was used to measure and calculate the residual stress on the surface of the sample, and due to data requirements, room temperature tensile testing was performed on the samples with a strain rate of 1.0 mm/min. The pulsed laser ablation (PLA) experiment was carried out on the Ti60 alloy sample. The process parameters were as follows: laser power 0.4 kW, spot diameter 2.4 mm, defocus 0 mm, and ablation time 5 s. A Nova Nano 450 field emission scanning electron microscope (SEM) was used to observe and analyze the microstructure before and after ablation. SEM and energy dispersive spectroscopy (EDS) were used to analyze the compositions of the elements.

3 Results and discussion

3.1 Effect of UIT on microstructures of LSFed Ti60 alloy

The macroscopic surface morphology before and after UIT is shown in Fig. 2. Many powder particles are splashing on the surface of the laser deposition layer in Fig. 2(a), and the phenomenon of sticky powder is serious. The average surface roughness perpendicular to the scanning direction is about 30 μm. The average surface roughness of the samples after UIT is 12 μm, which is reduced by 60%, as shown in Fig. 2(b). This is because the local surface tissue of the deposition layer is loose. After the high-frequency impact of the impact gun, the Ti60 surface is covered with fish-scale impact marks, and plastic deformation occurs on the surface of the deposition layer, making the internal structure denser. Finally, comparing the height of the deposited layer before and after UIT, it can be found that it is 3.17 mm before UIT and 2.86 mm after UIT, and the deformation caused by UIT is about 10%.

As shown in Fig. 3(a), the middle region of the LSFed Ti60 alloy sample was mainly composed of β-columnar crystals growing epitaxially along the deposition direction, and the microstructure at the bottom and top of the sample was mainly composed of a small number of equiaxed grains. As shown in

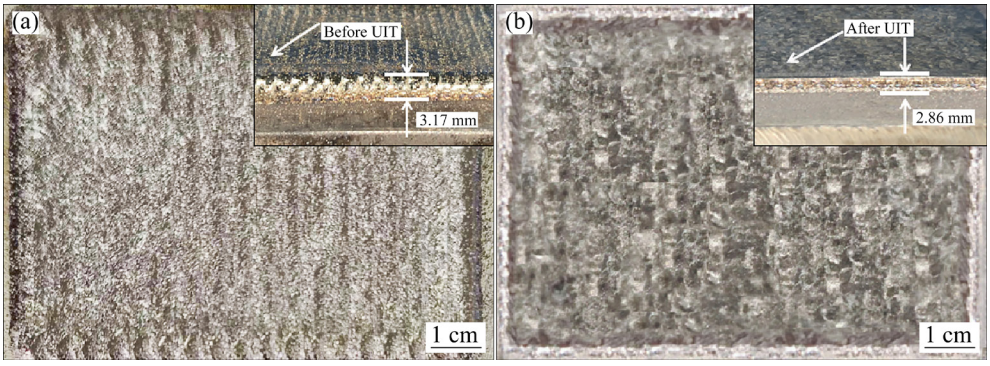

Fig. 2 Surface morphologies of Ti60 deposition layer: (a) Before UIT; (b) After UIT

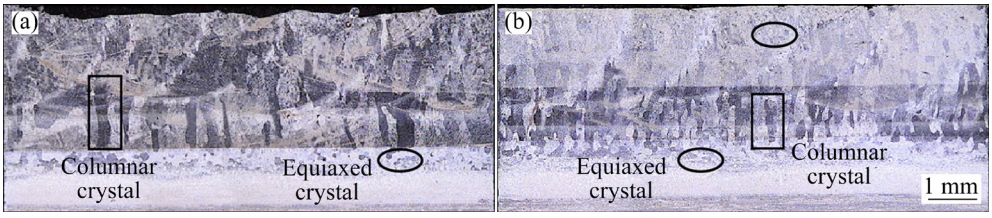

Fig. 3 Cross-section morphologies of LSFed Ti60: (a) Before UIT; (b) After UIT

Fig. 3(b), the grain size of the columnar crystals in the deposited layer was significantly reduced by the high-frequency impact of the impact needle, and some broken fine grains appeared after UIT.

The coarse columnar crystals in the middle of the sample were broken and reduced in size, and the surface of the sample was severely deformed. Moreover, the content of equiaxed crystals was increased. The reason is that UIT was performed on the surface of the LSF sample, which led to plastic deformation of the LSFed Ti60 deposited layer. During the LSF process, the refined grains acted as new nucleation particles to interrupt the epitaxial growth of β-columnar crystals and refine the grains. However, in the subsequent LSF process, there is some thermal effect on the microstructure in the lower and middle regions, so there is still a small amount of columnar structure. From the effect of UIT on the organization of the LSFed Ti60 deposited layers mentioned above, it can be seen that UIT treatment of each deposited layer can not only change the microstructure of the top layers significantly but also the bottom layers, improving the overall properties of the deposited layers.

In Fig. 4(a), there are some porosity defects in the overlap area at the top of the sample before UIT. Figures 4(a_1) and (a_2) show the local magnified views of the pores in the upper and lower parts of Fig. 4(a). The distribution of pores with different sizes was observed because the gas did not escape in time during the solidification process. Studies have shown that the formation of pores is ultimately derived from the gas within the melt pool, including the presence of gaseous elements in the hollow powder itself and argon gas rolled into the melt pool with the powder. When the gas enters the melt pool, the escape velocity of the gas is less than the solidification velocity of the solid−liquid interface of the melt pool, and the gas will be trapped by the solid−liquid interface and gas pores will be formed in the deposited layer [25].

Figures 4(b, b_1, b_2) show the pores after UIT and their local magnification. It can be observed that there are only tiny pores in the sample after UIT (Figs. 4(b_1) and (b_2)) compared with the sample before UIT and the large-size pores basically disappear. This is because the high-frequency and efficient impact of the UIT causes the deformation of the deposited layer. WU et al [26] found that the higher the impact energy obtained per unit length of the sample is, the more completely the pores are closed. Impact energy is closely related to the impact frequency, air pressure, speed, amplitude, etc. It can be seen that the higher the frequency, the more times of impact per unit length, and the greater the impact energy. At the same time, the UIT alters the original stress field, producing a certain amount of compressive stress. Therefore, the internal pores and defects of the formed parts are all reduced.

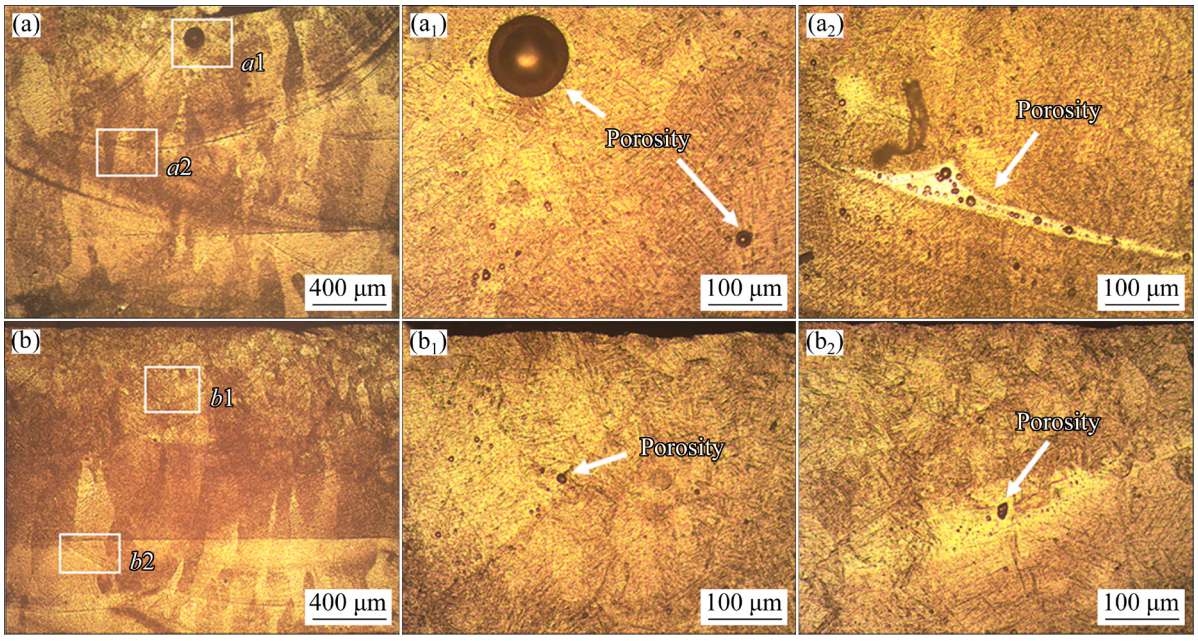

Fig. 4 Defects in deposition layer: (a) Top pores before UIT; (a_1, a_2) Local enlargement of pores before UIT; (b) Pores at top of interlayer after UIT; (b_1, b_2) Local enlargement of pores after UIT

To demonstrate the grain refinement effect of UIT on the surface of LSFed Ti60 alloy, the top area of the Ti60 samples before and after UIT was selected and samples with a diameter of 3 mm and a thickness of 0.1 mm were prepared in this study. The TEM images of the samples are shown in Fig. 5. Figure 5(a) shows the TEM image of Ti60 alloy before UIT, in which the white lath α phase and the black β phase can be clearly seen. The width of the lath α-phase is about 1.25 μm and that of the β-phase is about 50 nm. Figure 5(b) shows the dark field image of the β-phase between the laths, which is formed due to the faster cooling of the melt pool during the transition from the β-phase to the α-phase and the diffusion aggregation of solute atoms at the boundary of the lath α-phase. Figures 5(c) and (d) show the selected area electron diffraction (SAED) patterns of α-phase and β-phase, respectively. Figure 5(e) shows the TEM image after UIT, and the lath α structure cannot be observed. The grain is refiner than that of the sample before UIT. Regions *A* and *B* are selected for higher multiple observations. According to the measurement, the minimum grain size is about 40 nm, and the maximum grain size is less than 100 nm, which is significantly smaller compared to the coarse β-phase grains (>100 μm) that penetrate to the top before UIT. Figures 5(f) and (g) show that there are many high dislocation densities, dislocation entanglements, dislocation walls, and grains in this region, and the dislocation distribution is not uniform. The local high dislocation densities intertwine with each other, forming dislocation entanglement. The number of dislocations in the original grains gradually increases after UIT and rearranges to a certain extent to reduce the energy configuration, resulting in the formation of dislocation walls. Finally, the dislocation wall and dislocation tangles gradually evolve into grain boundaries. Consequently, coarse grains are differentiated into many sub-grains with different morphologies. Similar evolutionary processes are repeated under the influence of UIT, and finally randomly oriented equiaxed nanocrystalline layers are formed.

Region *A* is selected for analysis. In Fig. 5(h), the selected electron diffraction points show relatively continuous polycrystalline diffraction rings, which are typical nanocrystalline diffraction patterns. Comparison with the PDF card reveals that the diffraction rings all correspond to the α-phase, which is similar to that of XRD because of the minimal β content in the near-α titanium alloy. This strongly supports the role of UIT technology in the grain refinement, which is the formation of nanocrystals on the surface of the sample. According to the subsequent mechanical property analysis, the surface nanocrystalline layer improves the surface strength and burn resistance properties of the material.

Therefore, it is proven that UIT can significantly reduce the grain size of the LSFed Ti60 alloy and form a nanocrystalline layer on the surface.

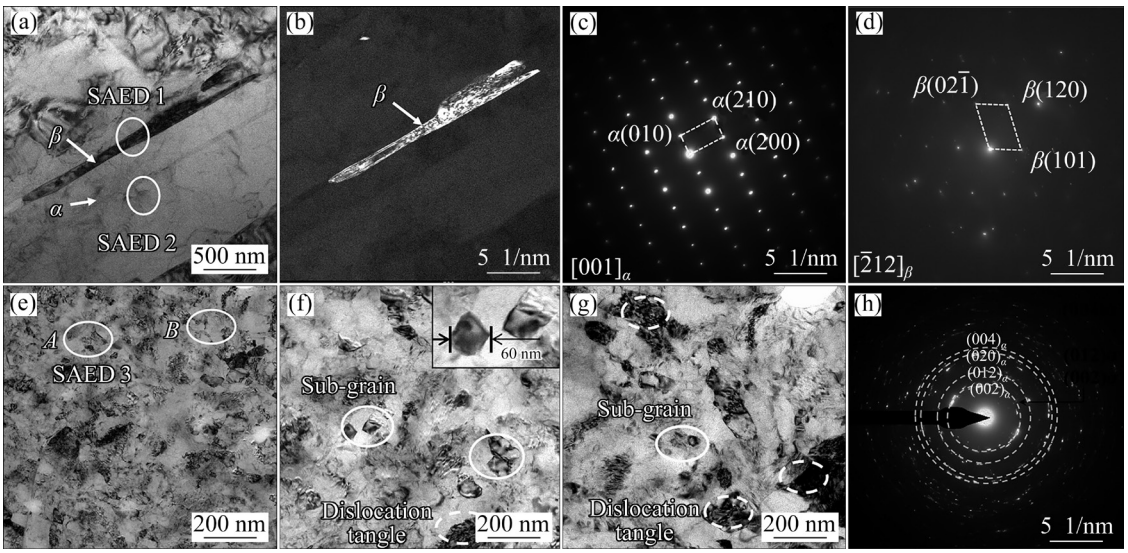

Fig. 5 TEM images of LSFed Ti60 alloy at 0.1 mm from surface: (a, b) Before UIT; (c) SAED 1; (d) SAED 2; (e) After UIT; (f) Enlarged view of Region *A*; (g) Enlarged view of Region *B*; (h) SAED 3

3.2 Effect of UIT on phases of LSFed Ti60 alloy

XRD has been widely used in the analysis of the phase composition of the material and grain size because it has the advantages of no damage, no pollution, and fast detection. To further analyze the phase composition and grain refinement mechanism of the nanocrystals detected above, XRD patterns of the as-deposited Ti60 alloy and the surface of the deposition layer after UIT were measured.

As shown in Fig. 6, the main phase of the LSFed Ti60 sample is α-Ti. Ti60 is a near-α high-temperature titanium alloy that contains a small number of β-stabilizing elements. Moreover, LSFed Ti60 is mainly a basketweave organization consisting of lath α-phase and little β-phase. Therefore, only α-Ti can be detected on the surface of the sample. The diffraction peak distribution of the Ti60 deposition layer is similar to that of the layer before UIT, indicating that there is no phase transition in the deposition process. The sample before UIT is indicated by the black line, and the sample after UIT is indicated by the red line. The main peaks of the XRD patterns of the samples after UIT correspond to those of the LSFed samples. Compared to that of the sample before UIT, the diffraction peaks decrease obviously.

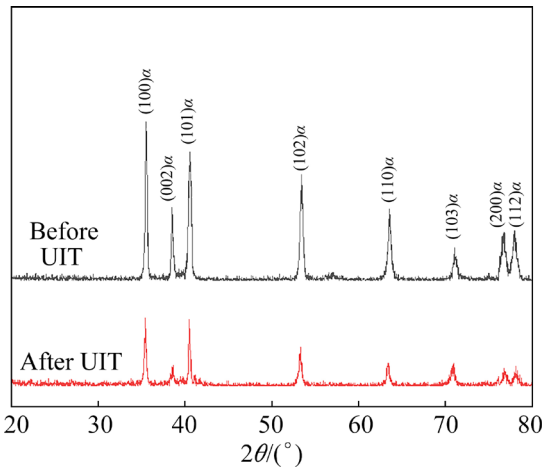

Fig. 6 XRD patterns of deposition layer before and after UIT

The height of the diffraction peak before UIT is greater than that after UIT, and the full width at half maximum (FWHM) is significantly reduced. The main factors affecting the FWHM include grain size, dislocation density, microscopic stress, and instrument width. According to Debye−Scherrer's formula:

$$L=\frac{K\lambda}{B\cos\theta} \tag{1}$$

where L is the normal length of the grain reflector, i.e., grain size, K is the Scherrer's constant, λ is the X-ray wavelength, and θ is the crystal plane Bragg angle. B is the half-width of the diffraction peak, that is, the angle range occupied when the intensity of the diffraction peak is half of the maximum value [27].

When K, λ, and θ are constant, the larger the FWHM (B) of the diffraction peak is, the smaller the grain size L is. It has been demonstrated that the deposited layer after UIT produces severe deformation. A large amount of dislocation proliferation, a significant increase in FWHM and a high degree of grain refinement are observed.

3.3 Effect of UIT on microhardness of LSFed Ti60 alloy

The hardness test of the impact layer section was carried out in the order from bottom to top, with a measurement spacing of 0.1 mm. Figure 7 shows the surface hardness distribution of the deposited layers after UIT, where the microhardness increases with increasing distance from the substrate. It should be noted that at a distance of less than or equal to 1 mm from the substrate, the microhardness of the LSFed sample increases as much as that of the UIT sample. When the distance between the test point and the substrate exceeds 1 mm, the microhardness of the sample after UIT increases more significantly than that of the LSFed

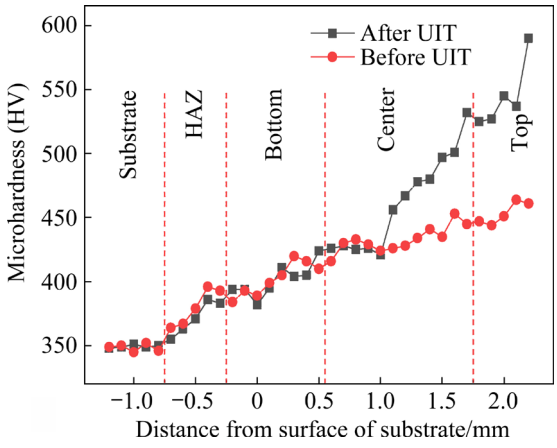

Fig. 7 Surface hardness distribution of deposited layer after UIT

sample. The maximum hardness of the sample after UIT is about HV 590, which is HV 130 higher than that of the LSFed sample (HV 460). That is to say, the microhardness gradually increases with decreasing distance from the surface of the deposition layer after UIT.

According to the pattern of the hardness distribution graph of the ultrasonic impacted Ti60 deposited layer, combined with the Hall−Petch formula, it is known that the reduction of average grain size can increase the hardness (H_V).

$$H_V=H_0+kd^{-1/2} \tag{2}$$

where H_V is the hardness, H_0 is the initial hardness, k is the constant, i.e., influence coefficient of grain boundary on strength, and d is the average grain size.

As can be seen from Section 3.1, the coarse columnar crystals (>100 μm) grow continuously in the middle of the sample. Columnar crystals break up and their sizes decrease after UIT. TEM results show that the grain size of the top layer of the LSFed Ti60 alloy impact sample is refined to be lower than that of the middle layer, and even reaches the nanometer level (40−100 nm). At the same time, the surface microhardness reaches its maximum, and the surface hardness is significantly higher than the central part, so it is in accordance with the Hall−Petch formula.

The increase in hardness after UIT can be attributed to the refinement strengthening and dislocation strengthening. With the grain refinement, the number of grain boundaries per unit volume increases, and the atoms at the grain boundaries are disordered, and the dislocation density is higher, resulting in an increase in the deformation resistance of the material.

3.4 Influence of UIT on residual stress of LSFed Ti60 alloy

The residual stress of the LFS deposition layer is mainly affected by three parts: phase transition stress during the heating process of the molten pool, quenching stress during the solidification process of the molten pool, and thermal stress generated when the deposition layer and the matrix cool together at the end of solidification [28,29]. The residual stress will reduce the mechanical properties and fatigue strength of the AM metal, resulting in material failure [30]. In this experiment, the Vickers hardness indentation method was used to measure the residual stress of the Ti60 alloy for a qualitative analysis of the experiment. This method has been used by many authors in other papers. WANG et al [31] used the Vickers indentation to evaluate the surface residual stress and hot hardness of spheroidizing annealing processed samples. CARLSSON and LARSSON [32] conducted Vickers indentation test on bending test samples. It is found that the residual stress field can well be correlated with the ratio of the actual to nominal contact areas at the indentation. The method is divided into the following steps. Firstly, the tensile test of the LSFed Ti60 alloy is carried out at room temperature; MATLAB mathematical software is used to fit the stress−strain curve to obtain the exponential relationship equation of stress and strain. Secondly, the Vickers microhardness is measured and the measurement results are shown in Section 3.3. Thirdly, the diagonal hardness indentation and the actual contact projection area are measured. Fourthly, the data obtained from the above steps are substituted into the residual stress calculation equation to obtain the residual stress values at the corresponding positions.

Figure 8(a) shows the tensile stress−strain curve and power exponential function fitting curve parameters of the LSFed Ti60 alloy sample. The fitted curve conforms to the Hollomon relation, where $S=K_1\varepsilon^n$ (S and ε are the actual stress and strain in the tensile strength curve, respectively; K_1 and n are the strength coefficient and strain hardening index of the material, respectively). The values are K_1=1323.708 and n=0.054. The parameter C^2 of the indentation area ratio is introduced to characterize the amount of metal accumulation around the indentation, $C^2=A/A_{nom}$ (A is the actual area and A_{nom} is the apparent area).

By substituting the values of K_1, n, H_v, and C^2 into Eqs. (3) and (4) [31], the residual strain (ε_{res}) and residual stress (σ_{res}) at each hardness test site can be calculated as follows:

$$\varepsilon_{res}=\left(\frac{H_v}{3.4K_1}\right)^{1/n}-0.08 \tag{3}$$

$$\sigma_{res}=K_1\left|\varepsilon_{res}\right|^n\{\exp[(C^2-1)/0.32]-1\} \tag{4}$$

Figure 8(b) shows the distribution of residual stress from the bottom to the top of the sample before and after UIT. Before UIT, the distribution

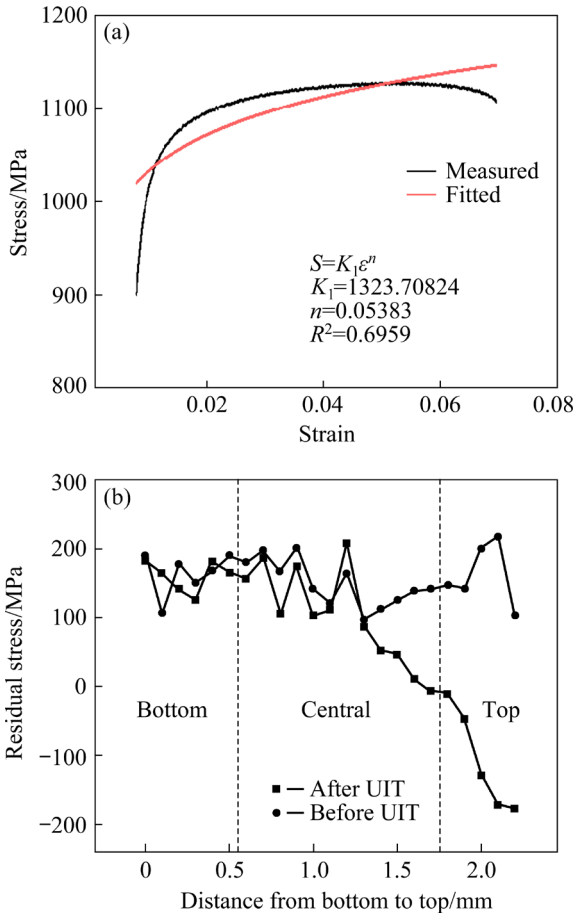

Fig. 8 Residual stress diagram of UIT section: (a) Tensile stress−strain curve and fitting parameters of power exponential function; (b) Residual stress before and after UIT

of residual stress in each region fluctuates between 100 and 250 MPa, and the maximum residual stress is located at the top of the sample. After UIT, the residual stress fluctuates steadily at a distance from 0 to 1.25 mm away from the substrate. When the distance from the substrate is above 1.25 mm, it starts to drop from 100 MPa and then rises back to −177 MPa, indicating that it changes from tensile stress to compressive stress. The change in the absolute value of residual stress before and after UIT is 277 MPa. The residual compressive stress can extend the fatigue life by stalling crack expansion and resisting some tensile stresses under external loads in use.

The maximum residual compressive stress exists in the plastic deformation layer on the surface. At the end of the plastic deformation depth, the residual stress approaches zero under the balance of the tensile stress field in the subsurface layer and the compressive stress field on the surface. This balance is achieved by the dislocations in the crystal and the combination of dislocation structure and arrangement. UIT causes the dislocations in the crystal to slip, resulting in strong plastic deformation, and repeated slipping and climbing of the dislocations in the crystal as the ultrasonic waves continue to act. Dislocations of opposite signs on the same slip plane cancel each other out and reduce the dislocation density within the sub-grain. Therefore, it can be assumed that the dislocation density in this region decreases under the action of huge impact energy after UIT, the energy is reduced, and the residual tensile stress is released.

3.5 Influence of UIT on burn resistance performance of LSFed Ti60 alloy

To test the high-temperature performance of Ti60, laser ablation (LA) [33] experiments were carried out on the Ti60 alloy sample before and after UIT to verify the burn resistance performance of the deposition layer. Pulsed laser ablation experiments can better simulate the characteristics of the thermal environment of Ti60 with high heat input in a very short period of time in the molten layer, and it can conveniently evaluate the ablation resistance of the material.

Figure 9(a) shows the surface morphology of the LSFed Ti60 sample after LA. From the surface edge to the center, there are an ablation zone, a heat-affected zone, and an oxidation zone in sequence. The size of the ablative pit with an irregular oval shape of the sample before UIT is larger, approximately 4.34 mm^2. In the process of LA, temperatures of thousands or even tens thousands of degrees can be generated near the focal point, and the surface of the Ti60 alloy sample boils off rapidly and evaporates, resulting in the formation of near-elliptical ablation pits. Figure 9(b) shows the LA surface morphology of the Ti60 sample under an impact pressure of 0.05 MPa. After UIT, the size of the ablation pit decreases significantly, and the shape is a regular circle. The heat-affected and oxidized zones have a more uniform surface, with more molten mixtures remaining in the ablation pits and less evaporation of the metal elements. The ablative surface is also smooth and dull in color.

Figure 9(c) shows the ablative areas of LA of Ti60 before and after UIT. The areas of the heat-

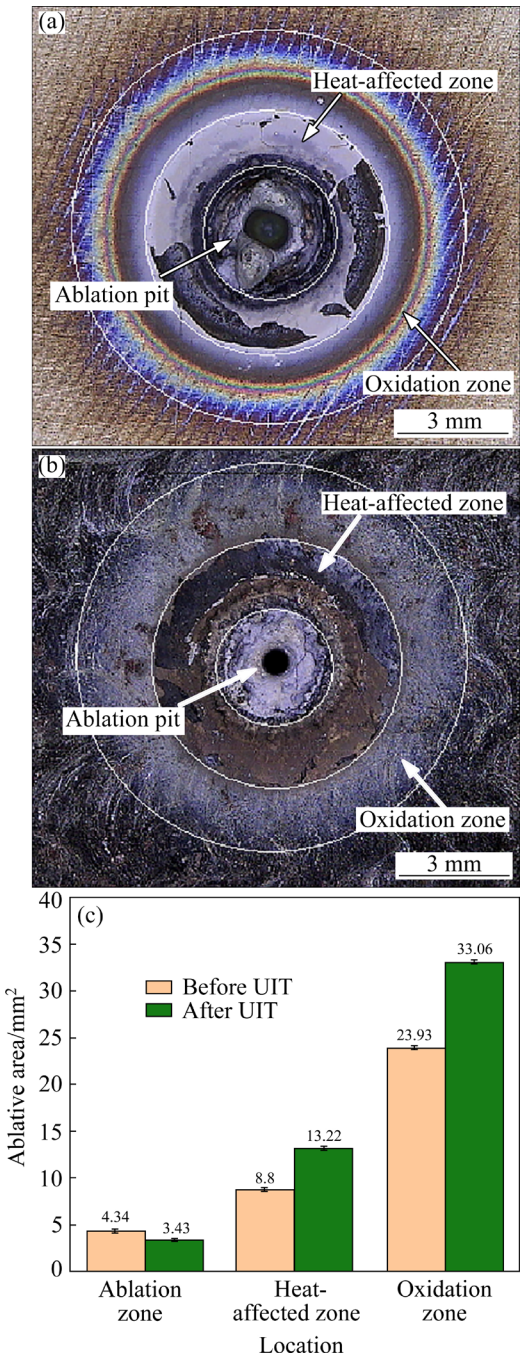

Fig. 9 Surface morphologies of LA before (a) and after (b) UIT, and statistical map of ablative areas before and after UIT (c)

affected zone and oxidation zone after UIT in Figs. 9(a) and (b) are both larger than those before UIT. This shows that the ablation pit area decreases, and the burn resistance effect is improved to a certain extent. The main factor to be considered in evaluating the excellent burn resistance performance is the size of the ablative pit area. Reducing the area of the ablation pit can improve the burn resistance.

To further explore the products of the LSFed Ti60 alloy under UIT-assisted LA and its burn resistance mechanism, SEM was used to observe the inner surface morphology of the ablation pit before and after UIT. Figure 10 shows the morphology of ablation pits before and after UIT. The regions *a*1 and *b*1 are oxides. It is found that oxides are distributed in the dense molten mixture after UIT. To clarify its composition and element changes, ablation areas *a*1 and *b*1 were detected by energy dispersive X-ray spectroscopy (EDS), and the results are shown in Table 4.

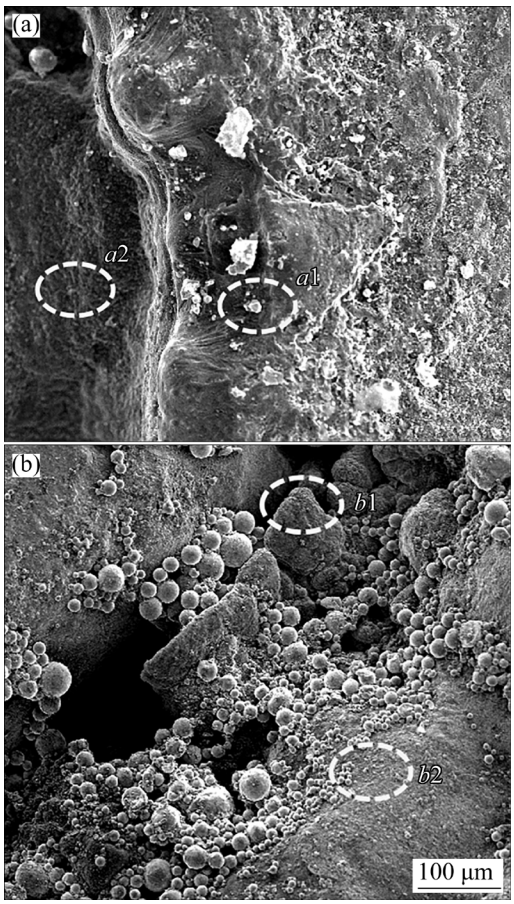

Fig. 10 Surface morphologies of ablation pits of LA Ti60 alloy: (a) Before UIT; (b) After UIT

As seen in Table 4, the particles of the sample before UIT are mainly composed of Ti and O, and the molar ratio is approximately 1:2, indicating that the surface of combustion products and the surface of attached particles are mainly composed of TiO_2. The contents of Mo, Si, and Nb increase after UIT. This is because a large amount of heat is generated on the surface of the Ti60 deposited layer during the UIT process, resulting in the evaporation and escape of elements with lower melting points on the

Table 4 EDS results of LSFed Ti60 alloy by LA

Process	Area	Content/at.%								
		O	Ti	Al	Zr	Mo	Nb	Ta	Si	Sn
Before	*a*1	67.7	29.5	1.9	1.2	−	−	−	−	−
UIT	*a*2	69.6	27.8	2.1	0.5	−	−	−	−	−
After	*b*1	64.3	30	2.6	1.8	0.3	0.3	−	0.4	−
UIT	*b*2	62.2	31.8	3.1	2.2	0.2	0.4	−	0.1	−

surface of the deposited layer. This indirectly increases the proportion of burn resistance elements such as Mo, Nb, and Zr on the deposited surface layer. This shows that the loss of alloying elements of the sample after UIT is decreased, which improves its burn resistance properties. ZHANG et al [16] and LI et al [34] concluded that there are two ways to improve the ablation resistance of titanium alloys: increasing the proportion of *β*-phase in the organization of complex-phase titanium alloys and adding some burn resistant elements. GUO et al [35] found that Mo with a mass fraction of 0.6% improves the thermal stability of titanium alloys. ZHU [36] has shown that Nb forms a stable Ti-rich nitride layer at the metal−oxide interface, which hinders the transport of anions and cations, and that the optimal content of Ta is 0.5−1.0 at.%. Therefore, the samples after UIT have less loss of alloying elements after ablation, more generation of a dense oxide protective layer on the surface of ablation pits, and better burn resistance properties. At the same time, dislocations continuously move and accumulate to form dislocation walls during UIT, and with increasing plastic strain, sub-grain boundaries are formed, which gradually evolve to the short axis and finally form dense nanocrystalline layers on the Ti60 surface. The dense nanocrystalline layer hinders the diffusion of oxygen into the alloy during laser ablation. It reduces the burning rate of alloying elements and improves the burn resistance property of the Ti60 deposition layer. Preventing oxygen diffusion during the LA process means that the dense structure of the metal surface created by UIT prevents further oxidation reactions and enhances the burn resistance properties. However, the mechanism of this diffusion effect is different from that of severe plastic deformation. Diffusion enhancement due to severe plastic deformation means that most of the second phase is incorporated into the matrix in a concise period.

4 Conclusions

(1) The surface roughness of the LSFed Ti60 deposition layer was reduced by 60% by UIT, and severe deformation was generated. The equiaxed grains on the surface and at the bottom increased significantly. After the UIT process, the internal pores were reduced to a certain extent. The continuous coarse columnar crystals were broken, the number of equiaxed crystals increased, and a layer of nanocrystals was formed on the surface. XRD analysis shows the UIT induced decrease of the grain size in sub-surface layers. It proves that the effect of UIT on grain refinement is significant.

(2) UIT improved the microhardness of the intermediate and surface layers, increasing the maximum hardness value by HV 130. At the distance of 1.25 mm from the substrate, the residual stress dropped from 100 MPa and then rose back to −177 MPa, which significantly reduced the residual stress in the middle and top of the sample, releasing the residual tensile stress, and obtained the compressive stress.

(3) It is demonstrated that the burn resistance property of the Ti60 alloy is improved after UIT from three aspects. Firstly, the area of the ablation pit was reduced by 21% after UIT. Secondly, the increasing proportion of burn resistant elements such as Mo, Si, and Nb after UIT indirectly leads to an increase in the oxide protective layer content. Thirdly, the diffusion of oxygen was hindered by the dense nanocrystalline layer formed on the Ti60 deposited layer after UIT.

Acknowledgments

This work is financially supported by the National Natural Science Foundation of China (No. 52165050), and the Natural Science Foundation of Jiangxi Province, China (No. 20181BAB206027).

References

[1] CAI Jian-ming, TIAN Feng, LIU Dong, LI Juan, MI Guang-bao, YE Jun-qing. Research progress in manufacturing technology of 600 °C high temperature titanium alloy dual property blisk forging [J]. Journal of Materials Engineering, 2018, 46(5): 36−43. (in Chinese)

[2] LI Wen-yuan, CHEN Zhi-yong, LIU Jian-rong, WANG Qing-jiang, SUI Guo-xin. Effect of texture on anisotropy at 600 °C in a near-*α* titanium alloy Ti60 plate [J]. Materials Science and Engineering A, 2017, 688: 322−329.

[3] ZHANG A-li, LIU Dong, TANG Hai-bo, WANG Hua-ming. Microstructure evolution of laser deposited Ti60A titanium alloy during cyclic thermal exposure [J]. Transactions of Nonferrous Metals Society of China, 2013, 23: 3249−3256.

[4] CHEN Wei, ZENG Wei-dong, XU Jian-wei, ZHOU Da-di, WANG Si-min, HE Sheng-tong. Deformation behavior and microstructure evolution during hot working of Ti60 alloy with lamellar starting microstructure [J]. Journal of Alloys and Compounds, 2019, 792: 389−398.

[5] ZHANG Qiang, CHEN Jing, TAN Hua, LIN Xin, HUANG Wei-dong. Microstructure evolution and mechanical properties of laser additive manufactured Ti−5Al−2Sn−2Zr−4Mo−4Cr alloy [J]. Transactions of Nonferrous Metals Society of China, 2016, 26: 2058−2066.

[6] FU Mao-sen, YUAN Ya-ru, MA Xiao, LIN Xin. A study of α variant selection in laser solid forming Ti−6Al−4V [J]. Journal of Alloys and Compounds, 2019, 792: 1261−1266.

[7] WANG Wen-chang, LI Jia-xing, GE Yuan, KONG De-jun. Structural characteristics and high-temperature tribological behaviors of laser cladded NiCoCrAlY−B_4C composite coatings on Ti_6Al_4V alloy [J]. Transactions of Nonferrous Metals Society of China, 2021, 31: 2729−2739.

[8] YAN Wen-gao, WANG Hua-ming, TANG Hai-bo, CHENG Xu, ZHU Yan-yan. Effect of Nd addition on microstructure and tensile properties of laser additive manufactured TC11 titanium alloy [J]. Transactions of Nonferrous Metals Society of China, 2022, 32: 1501−1512.

[9] BOYER R R. An overview on the use of titanium in the aerospace industry [J]. Materials Science and Engineering A, 1996, 213(1): 103−114.

[10] LEUDERS S, THÖNE M, RIEMER A, NIENDORF T, TRÖSTER T, RICHARD H A, MAIER H J. On the mechanical behaviour of titanium alloy $TiAl_6V_4$ manufactured by selective laser melting: Fatigue resistance and crack growth performance [J]. International Journal of Fatigue, 2013, 48: 300−307.

[11] MERCELIS P, KRUTH J P. Residual stresses in selective laser sintering and selective laser melting [J]. Rapid Prototyping Journal, 2006, 12(5): 254−265.

[12] CHENAKIN S P, MORDYUK B N, KHRIPTA N I. Surface characterization of a ZrTiNb alloy: Effect of ultrasonic impact treatment [J]. Applied Surface Science, 2018, 470: 44−55.

[13] KAHRAMAN F. Surface layer properties of ultrasonic impact-treated AA7075 aluminum alloy [J]. Journal of Engineering Manafacture, 2018, 232(12): 2218−2225.

[14] SONG Bo, DU Zhi-wen, YANG Qing-shan, GUO Ning, GUO Sheng-feng, YU Jin-cheng, XIN Ren-long. Effect of pre-rolling path on mechanical properties of rolled ZK60 alloys [J]. Transactions of Nonferrous Metals Society of China, 2021, 31: 1322−1338.

[15] WU Shu-xu, WANG Shou-ren, WANG Gao-qi, YU Xiu-chun, LIU Wen-tao, CHANG Zheng-qi, WEN Dao-sheng. Microstructure, mechanical and corrosion properties of magnesium alloy bone plate treated by high-energy shot peening [J]. Transactions of Nonferrous Metals Society of China, 2019, 29: 1641−1652.

[16] ZHANG Xiao-yu, HUANG Sheng, LI Di-chen, GENG Jia-le, YANG Fan, LI Qing-yu. An approach to improve the microstructure and mechanical properties: A hybrid manufacturing of laser directed energy deposition and shot peening [J]. Additive Manufacturing, 2022, 55: 102686.

[17] ZHANG Yao-zu, HUANG Chun-ping, LIU Feng-gang, LIU Feng-cheng, SONG Meng-hua, KE Li-ming. Nano-crystallization of a Ti40 cladding layer by ultrasonic impact to improve burn resistance [J]. Journal of Materials Research and Technology, 2021, 11: 1331−1342.

[18] WANG Yu-ling, LI Cheng, JIANG Fu-lin, ZHANG Jie, AN Xiang-long. Microstructure and mechanical properties of ultrasonic assisted laser cladding Al_2O_3−ZrO_2 ceramic coating [J]. Materials Research Express, 2019, 49(11): 309−319.

[19] LESYK D A, MARTINEZ S, MORDYUK B N, DZHEMELINSKYI V V, LAMIKIZ A, PROKOPENKO G I. Post-processing of the Inconel 718 alloy parts fabricated by selective laser melting: Effects of mechanical surface treatments on surface topography, porosity, hardness and residual stress [J]. Surface and Coatings Technology, 2020, 381: 125136.

[20] YU Ying-xia, HE Bo-lin, LV Zong-min, LEI Si-yong, XIA Song-song. Experimental research on microhardness and wear resistance of MB8 magnesium alloy treated by ultrasonic impact [J]. Rare Metal Materials and Engineering, 2017, 46(7): 1798−1802.

[21] YANG Yi-chong, JIN Xin, LIU Chang-meng, XIAO Mu-zheng, LU Ji-ping, FAN Hong-li, MA Shu-yuan. Residual stress, mechanical properties, and grain morphology of Ti−6Al−4V alloy produced by ultrasonic impact treatment assisted wire and arc additive manufacturing [J]. Metals, 2018, 8(11): 934.

[22] TRUDEL E, WALKER P, NOSIR S, ElSAYED M S A. Experimental optimization for fatigue life maximization of additively manufactured Ti−6Al−4V alloy employing ultrasonic impact treatment [J]. Journal of Materials Engineering and Performance, 2021, 30(4): 2806−2821.

[23] DONOGHUE J, SIDHU J, WESCOTT A, PRANGNELL P. Integration of deformation processing with additive manufacture of Ti−6Al−4V components for improved β grain structure and texture [C]//TMS 2015 144th Annual Meeting & Exhibition. Cham: Springer, 2015: 437−444.

[24] ZHAO Xue-sen, ZHAO Dong-xu, HU Wang-jie, ZHANG Junjie, WANG Xiao-hui, ZHANG Jian-guo, SUN Tao. Manufacturing of high-precision surface micro-structures on stainless steel by ultrasonic impact peening [J]. The International Journal of Advanced Manufacturing Technology, 2021, 116: 915−930.

[25] KEMPEN K, THIJS L, HUMBEECK J V, KRUTH J P. Processing $AlSi_{10}Mg$ by selective laser melting: Parameter optimisation and material characterization [J]. Materials Science and Technology, 2015, 31(8): 917−923.

[26] WU Yong, DENG Wei, LIU Kai, ZHANG Zhi-lai, WU Di-peng, BO Jiu-yang. Effect of interlayer ultrasonic peening on the microstructure and mechanical properties of 2219 aluminum alloy by TIG wire arc additive manufacturing [J]. Aeronautical Science & Technology, 2021, 32 (11): 80−86. (in Chinese)

[27] DAI Shi-juan, ZHU Yun-tian, HUANG Zhao-wen. Microstructure evolution and strengthening mechanisms of

pure titanium with nano-structured surface obtained by high energy shot peening [J]. Vacuum, 2016, 125: 215−221.

[28] FARAHMAND P, KOVACEVIC R. An experimental−numerical investigation of heat distribution and stress field in single- and multi-track laser cladding by a high-power direct diode laser [J]. Optics & Laser Technology, 2014, 63: 154−168.

[29] YE He, LE Fang-bin, WEI Chao, YE Kun, LIU Sen-zhong, WANG Guan-ming. Fatigue crack growth behavior of Ti−6Al−4V alloy fabricated via laser metal deposition: Effects of building orientation and heat treatment [J]. Journal of Alloys and Compounds, 2021, 868: 159023.

[30] COLEGROVE P A, DONOGHUE J, MARTINA F, GU J L, PRANGNELL P, HÖNNIGE J. Application of bulk deformation methods for microstructural and material property improvement and residual stress and distortion control in additively manufactured components [J]. Scripta Materialia, 2017, 135: 111−118.

[31] WANG Yu-jie, CHU Shuang-jie, MAO Bo, XING Hui, ZHANG Jiao, SUN Bao-de. Microstructure, residual stress, and mechanical property evolution of a spray-formed vanadium-modified high-speed steel processed by post-heat treatment [J]. Journal of Materials Research and Technology, 2022, 18: 1521−1533.

[32] CARLSSON S, LARSSON P L. On the determination of residual stress and strain fields by sharp indentation testing. Part II: Experimental investigation [J]. Acta Materialia, 2001, 49: 2193−2203.

[33] YE Hao, HUANG Yin-bo, WANG Chen, LIU Guo-rong, LU Xing-ji, CAO Zhen-song, HUANG Yao, QI Gang, MEI Hai-ping. Measurement of uranium isotope ratio by laser ablation absorption spectroscopy [J]. Acta Physica Sinica, 2021, 70(16): 163201. (in Chinese)

[34] LI Bo, SHEN Yi-fu. Ti−Cu flame-retardant modified layer prepared by friction stir processing on surface of TC4 Ti alloy [J]. The Chinese Journal of Nonferrous Metals, 2018, 28: 435. (in Chinese)

[35] GUO Jia-lin, DONG Yan-ni, YUE Xu, CHEN Bing-gang, WANG Ding-chun, LIU Jian-rong, WANG Qing-jiang. Effect of molybdenum on microstructure and mechanical properties of high temperature titanium alloy working at 650 ℃ [J]. Nonferrous Metal Materials and Engineering, 2018, 39(2): 6−11. (in Chinese)

[36] ZHU Shao-xiang. Effect of isomorphous β-stabilizing elements on microstructures and oxidation resistance of high temperature titanium alloy [D]. Shenyang: Shenyang University, 2019. (in Chinese)

激光立体成形和超声冲击混合制造 Ti60 合金的显微组织和性能

陈文婧[1]，黄春平[1]，刘丰刚[1]，梁仁瑜[1]，刘奋成[1]，杨海欧[2]

1. 南昌航空大学 轻合金加工科学与技术国防重点学科实验室，南昌 330063；
2. 西北工业大学 金属高性能增材制造与创新设计重点实验室，西安 710072

摘 要：采用激光立体成形(LSF)和超声冲击处理(UIT)混合制造的方法，通过逐层强化表面，改善 Ti60 合金的结构和性能。采用 SEM、TEM 和 XRD 分析并比较 UIT 前后 LSF 处理 Ti60 样品的显微组织、力学性能和阻燃性能。结果表明，UIT 后 LSF 处理 Ti60 合金的晶粒得到细化，冶金缺陷减少。同时，UIT 后沉积层严重变形，并在表面形成纳米晶体。此外，沉积层表面显微硬度提高，残余应力由拉应力变为压应力。烧蚀坑面积减少了 21%，Mo，Nb 和 Zr 元素的比例增加。综上所述，LSF 和 UIT 的混合制造可以改善 LSF 处理 Ti60 样品的显微组织和性能。

关键词：Ti60 合金；超声冲击处理；激光立体成形；显微组织；力学性能；阻燃性能

(Edited by Wei-ping CHEN)